Inelastic x-ray scattering in the vicinity of xenon L_3 edge

M. Žitnik, M. Kavčič, K. Bučar, A. Mihelič, M. Štuhec, and J. Kokalj

J. Stefan Institute, P.O. Box 3000, SI-1001 Ljubljana, Slovenia

J. Szlachetko

Physics Department, University of Fribourg, CH-1700 Fribourg, Switzerland and
Swietokrzyska Academy, Institute of Physics, 25-406, Kielce, Poland

A series of x-ray emission spectra of xenon in the region of $L_3M_{5,4}(L\alpha_{1,2})$ and $L_3N_{5,4}(L\beta_{2,15})$ lines were recorded along the polarization direction of the incoming photons with energies ranging from 4779.4 to 4804.4 eV. A combination of monochromatic photon beam and high resolution x-ray spectrometer resulted in the experimental broadening of 1 eV allowing the observation of resonantly enhanced and narrowed emission lines from the decay of $[2p_{3/2}]nd,ns$ states. The measured spectra are decomposed into the continuum and resonant contributions to determine their relative emission strengths and the energies of the lowest resonant excitations converging to the L_3 edge. The calculated differential cross section for inelastically scattered photons is compared to the measured data. Each of the resonant states is described by a single relativistic configuration in the frame of the Dirac-Fock model, and the continuum contribution to the scattered light is evaluated within the Caldwell-Zare approach, which neglects anisotropic interaction of the ejected electron with the ion.

I. INTRODUCTION

Two important tasks of atomic physics are to find out transition energies and strengths and to improve the models aiming to describe atomic reactions against the external perturbations. One of the most useful tools in this respect are the photoabsorption measurements. Energy dependence of the photoabsorption cross section displays characteristic steps which belong to excitations of an inner-shell electron passing into the continuum. Superimposed are many weak structures, the fingerprints of multielectron excitations and their respective thresholds. For the rare gas targets, these can be studied in detail since they are relatively easy to handle experimentally and to treat theoretically due to the closed shell symmetry of the atomic ground state [1–7]. The energy width of the structures in these spectra reflects the natural width of an inner hole created by photon absorption, similarly to the x-ray photoelectron spectroscopy (XPS), where the ejected electron yield is measured as a function of electron energy (e.g., [8]). Complementary to these are the methods for observing channels along which the excited states release the energy, mostly by Auger decay (AES) or x-ray emission (XES).

The available resolving power of spectrometers can be fully exploited in experiments where the energy resolution is not limited by the lifetime of the hole—the resonant Raman effect. Let the photon beam with Gaussian energy distribution impinge onto the atomic (ground state) target:

$$A(0) + \gamma(\sigma_p) \to A^*(\Gamma_i) \to A^*(\Gamma_f) + \gamma(\sigma_s).$$

We assume that resonantly scattered photons are detected by the spectrometer with Gaussian-like transmission function in energy. Due to energy conservation in the reaction the width of the measured emission line depends only on the total experimental width $\Gamma_{\text{expt}} \approx 2.35\sqrt{\sigma_p^2 + \sigma_s^2}$ and on the energy

broadening of the final atomic state Γ_f. Since the latter pertains to the more relaxed state, it is usually smaller than the natural width of the intermediate state Γ_i and spectral structures in the emission can be in principle better resolved than in the absorption [9]. This effect is most easily seen in the narrow band excitation of discrete states when observing Auger electrons [10–13], or x rays [14–18] emitted in the fast decay of an atomic inner-hole from in the solids, liquids and gases. The spectral line profiles and intensities depend on the electronic structure of the intermediate states and are sensitive to the precise energy and bandwidth of the incident x-ray beam in all the near ionization threshold region. X-ray emission cannot be treated there separately from the absorption process itself; a scattering formalism must be used.

To date, most of the experimental papers on x-ray resonant Raman scattering in noble gases have shown relatively few isolated spectra above and below the inner shell thresholds, except for the systematic study around Xe L_3 edge [19], which followed the evolution of $L_3M_{5,4}(L\alpha_{1,2})$ and $L_3N_{5,4}(L\beta_{2,15})$ emission lines with the incoming photon energy. The total experimental width was 2.6 eV, comparable to the natural linewidth Γ_i of the $2p_{3/2}$ hole [20]. The conclusions are very general, saying that the results are consistent with the theoretical descriptions of Tulkki and Åberg in terms of full transition matrix elements and generalized Kramers-Heisenberg scattering cross sections [21], although no quantitative comparison is made. Later on, the same group measured the evolution of spectator and diagram $L_3 - M_{45}M_{45}$ Auger intensities across the L_3 threshold, reaching the experimental resolution of about 1.9 eV [22]. By using the calculated multiplet structure the intensity dependence of the three contributions (based on $[2p_{3/2}]5d$, $[2p_{3/2}]nd(n > 5)$ and $[2p_{3/2}]$ intermediate states) was extracted from the measured data and successfully reproduced by the model. A delayed onset of the diagram line intensity due to the shake

TABLE I. The calculated and converged (bold) energies of atomic (i) and ionic (I) intermediate and final states (f, F) in comparison with previously published data. Reported are also the calculated oscillator strengths (gf) and both the calculated and converged (bold) emission strengths f_{0if}, f_{0IF}, and $(\partial f/\partial\epsilon)_{0IF}$ relative to the $0\to[2p_{3/2}]\to[3d_{5/2}]([4d_{5/2}])$ continuum emission strength $(\partial f/\partial\epsilon)_{0IF}=1.2\times10^{-10}(1.4\times10^{-11})$ a.u. The error estimates from the fit are given in round parentheses. (*) The uncertainty of the energy calibration is 0.25 eV.

$\lvert i\rangle$ $J_i=1$	E_i-E_0 calc.[eV]	E_i-E_0 fit* [eV]	E_i-E_0 others [eV]	$(gf)_{0i}$ calc.		
$[2p_{3/2}]5d_{5/2,3/2}$	4785.57	**4784.72(1)**	4784.2 [24]	1.24(−3), 1.35(−5)		
$[2p_{3/2}]6d_{5/2,3/2}$	4786.36	**4785.74(1)**	4785.3 [24]	6.08(−4), 4.08(−6)		
$[2p_{3/2}]7d_{5/2,3/2}$	4786.73		4785.7 [24]	2.93(−4), 1.20(−6)		
$[2p_{3/2}]6s_{1/2}$	4783.91	**4782.97(3)**	4782.4 [24]	1.27(−4)		
$[2p_{3/2}]7s_{1/2}$	4786.52			2.65(−5)		
$\lvert I\rangle$	E_I-E_0	E_I-E_0	E_I-E_0			
$[2p_{3/2}]$	4787.27	**4786.67(2)**	4786.3(6)[24] 4786.8(5)[29] 4787.34[32]			
$\lvert f\rangle$ $J_f=1,2$	E_f-E_0	E_f-E_0	E_f-E_0	$(gf)_{if}$ spectator	f_{0if} (calc.) $0\to i\to f$	f_{0if}(fit) $0\to i\to f$
$[3d_{5/2}]5d_{5/2,3/2}$	674.67	**674.67(1)**		0.99, 1.13	2.086	**2.460(5)**
$[3d_{5/2}]6d_{5/2,3/2}$	675.48	675.65		0.98, 1.15	1.008	**0.601(5)**
$[3d_{5/2}]7d_{5/2,3/2}$	675.85			0.97, 1.16	0.479	
$[3d_{5/2}]6s_{1/2}$	673.03	**672.94(1)**		1.20	0.256	**0.15(1)**
$[3d_{5/2}]7s_{1/2}$	675.64			1.20	0.053	
$[3d_{3/2}]5d_{5/2,3/2}$	687.33	**687.38(1)**		0.13, 0.10	0.254	**0.248(3)**
$[3d_{3/2}]6d_{5/2,3/2}$	688.13	688.41		0.13, 0.10	0.123	**0.070(5)**
$[3d_{3/2}]7d_{5/2,3/2}$	688.51			0.13, 0.10	0.059	
$[3d_{3/2}]6s_{1/2}$	685.51	**685.72(4)**		0.14	0.027	**0.02(1)**
$[3d_{3/2}]7s_{1/2}$	688.30			0.14	0.006	
$[4d_{5/2}]5d_{5/2,3/2}$	64.65	**65.54(1)**	67.548(1)[37]	0.11, 0.13	1.941	**2.40(2)**
$[4d_{5/2}]6d_{5/2,3/2}$	65.49	66.58		0.10, 0.13	0.865	**0.73(1)**
$[4d_{5/2}]7d_{5/2,3/2}$	65.88			0.10, 0.13	0.417	
$[4d_{5/2}]6s_{1/2}$	63.08	**63.86(1)**		0.13	0.235	**0.18(3)**
$[4d_{5/2}]7s_{1/2}$	65.68			0.14	0.050	
$[4d_{3/2}]5d_{5/2,3/2}$	66.63	**67.67(3)**	67.411(9)[37]	0.015, 0.011	0.244	**0.28(1)**
$[4d_{3/2}]6d_{5/2,3/2}$	67.46	68.54		0.014, 0.010	0.109	**0.07(1)**
$[4d_{3/2}]7d_{5/2,3/2}$	67.85			0.014, 0.010	0.500	
$[4d_{3/2}]6s_{1/2}$	65.04	**66.53(3)**		0.016	0.025	**0.09(1)**
$[4d_{3/2}]7s_{1/2}$	67.64			0.015	0.008	
$\lvert F\rangle$	E_F-E_0	E_F-E_0	E_F-E_0	$(gf)_{IF}$ spectator	$(\partial f/\partial\epsilon)_{0IF0}$ (calc.) $0\to I\to F$	$(\partial f/\partial\epsilon)_{0IF0}$ (fit) $0\to I\to F$
$[3d_{5/2}]$	676.48	676.65	676.70(8)[8] 677.42[32]	1.60	1.000	1.000
$[3d_{3/2}]$	689.13	689.37	689.35(8)[8] 690.11[32]	0.18	0.070	**0.088(3)**
$[4d_{5/2}]$	66.52	67.61	67.548(1)[37]	0.19	1.000	1.000
$[4d_{3/2}]$	68.48	69.57	69.537(2)[37]	0.021	0.067	**0.12(1)**

down of the slow photoelectron by the receding Auger electron was clearly observed, but, because the Auger diagram lines merge continuously into the high-n spectator distribution, there was no way to separate the spectator contribution by this non-coincidence experiment. On the other hand, the characterization of the intermediate states is more readily achieved by the x-ray resonant Raman experiment when $\Gamma_{\text{expt}}<\Gamma_i$ since, in principle, no postcollision interaction (PCI) effects are present [23] and the multiplet structure of the final states is simpler.
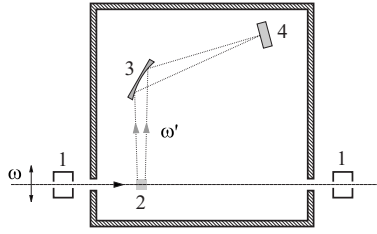
FIG. 1. A top-view scheme of the experimental setup: (1) ionization cell, (2) gas cell, (3) quartz crystal, and (4) CCD camera.

To our knowledge, the only published "experimental" energy positions of the discrete levels below the L_3 edge come from the analysis of the photoabsorption spectrum [24]. This was decomposed into the usual arctan continuum part and four Lorentzian profiles representing transitions into the $[2p_{3/2}]5-7d,6s$ discrete states with the Hartree-Slater method providing the initial fitting estimates. However, a large broadening of the $2p_{3/2}$ hole results in the relatively smooth and structureless absorption profile, so that it is difficult to rely on all the converged parameter values. The reported value of Xe L_3 binding energy is 4786.3 ± 0.6 eV, similar to other measurements (Table I), but for the discrete states neither line intensities nor the uncertainties of energy positions are given.

We have performed the resonant Raman experiment with the experimental broadening of the order of 1 eV achieved by a combination of the third generation synchrotron beamline and our new high resolution x-ray spectrometer [25]. This allowed a detailed analysis of $L_3M_{5,4}$ and $L_3N_{5,4}$ line evolutions across the Xe L_3 threshold. After reporting the experimental conditions, we describe a parametrization of Kramers-Heisenberg formula which is employed to extract the resonance energies and relative emission strengths from the experimental x-ray spectra. The (converged) experimental parameter values, which are the main result of this work, are compared to the calculated values obtained from the single configuration relativistic description of discrete states assuming a negligible interaction of the ejected electron with the residual ion.

II. EXPERIMENT

The measurements were performed at the x-ray absorption fine structure (XAFS) beamline of Elettra synchrotron. The horizontally polarized monochromatic photon beam with cross section 2×15 mm^2 and the flux of 10^{10} photons/s emerged from a double crystal Si (111) monochromator onto the gas target. The stainless steel gas cell was filled with Xe at 500 mbar and provided $b=10$ mm long interaction region (Fig. 1). This was separated from the spectrometer chamber by 12.5 μm thick kapton foils. The pressure inside the chamber with dimensions $1.6\times1.3\times0.4$ m^3 was kept at 1×10^{-6} mbar. Scattered photons were observed in the horizontal plane at 90° with respect to the direction of the incoming light. The quartz crystal with reflecting area of 70×30 mm^2 is cylindrically bent in Johansson geometry and has a Rowland circle radius of 500 mm. After the second

order diffraction on the $(10\bar{1}0)$ crystal planes, the photons were detected by the Peltier cooled(-40 °C) charge-coupled device (CCD) camera. The active area of the detector consist of 770×1153 pixels, each with the surface area of 22.5×22.5 μm^2, and allowed a precise localization of the x-ray events. The entrance to the camera was shielded by 6 μm thick mylar foil to reduce the detection noise.

The energy profile of the incoming light in the L_3 threshold region and the spectrometer transmission function in the $L_3M_{5,4}$ energy region are represented by Gaussians of 0.65 eV and 0.73 eV FWHM, respectively. These values emerged from an overall fitting procedure as described later. The linewidth of the $[2p_{3/2}]$ state is determined to be 2.62 ± 0.05 eV, which is in better agreement with 3.12 ± 0.16 eV, the linewidth of the L_3M_5 transition recently reported by Mauron et al. [26] (upon subtraction of 0.6 eV—the width of the final $[3d_{5/2}]$ state [20]) than with the recommended value of 2.82 eV [20]. In the region of $L_3N_{5,4}$ lines, the same procedure gives 0.59 eV for the Gaussian FWHM of the spectrometer. The total experimental width was therefore 1.0 eV in the $L_3M_{5,4}$ energy region and 0.94 eV in the $L_3N_{5,4}$ region and led to the substantial narrowing of the atomic emission lines. The latter estimate is consistent with the weak elastic peak profile recorded simultaneously with the $L_3N_{5,4}$ lines.

A series of 26 x-ray emission spectra was recorded in the energy region of $L_3M_{5,4}$ lines (4057–4153 eV), each at different incoming photon energy, starting at 4779.4 eV and increasing the excitation energy by 1 eV steps across the L_3 threshold, until reaching 4804.4 eV. The emission spectra are normalized to the same photon dose measured by continuous recording of the ion current in the ionization chamber in front of the target. The chamber was filled with a mixture of helium and nitrogen to absorb about 2% of the incident light, just enough for the monitoring purposes. Typical accumulation time was 2 h per spectrum, but could be as long as 5 h for the lowest photon energies. The second series of ten emission spectra was recorded in the energy region of $L_3N_{5,4}$ lines (4634–4796 eV) starting at 4780.4 eV and ending at 4789.4 eV incoming photon energy.

Before and after taking the series of emission spectra, the L_3 absorption spectrum was recorded. The partial pressures of helium-nitrogen gas mixture in the first ionization cell were set to achieve optimum measurement conditions. Measured absorption coefficient $\mu(\omega_0)$ was used to properly take into account the self-absorption in the gas cell. Each emission spectrum recorded at the nominal incoming photon energy ω_0 was therefore weighted by $\mu/(1-\exp[-\mu b])$, as appropriate for the perpendicular experimental geometry [27].

The energy scale of the emission spectra was calibrated by the reference position 4110.088(20) eV of L_3M_5 line [28] and checked by comparing the position of L_3M_4 line at 4097.33(3) eV with the reference value of 4097.378(30) eV [28]. The energy scale in the $L_3N_{5,4}$ energy region was calibrated against the reference energy position of 4718.86(8) eV [29]. The presence of the signal of elastically scattered photons in the same spectrometer window allowed a calibration of the energy of the incoming photons with uncertainty of 0.25 eV. The repeatability of the incoming

beam energy setting was verified several times during the measurements by recording the emission spectra at the same nominal energy.

III. PARAMETRIZATION

The differential cross section for photons with polarization $\hat{\boldsymbol{\epsilon}}_0$ and energy ω in the vicinity of the threshold I which are inelastically scattered into the solid angle $d\Omega'$ with energy ω' and polarization $\hat{\boldsymbol{\epsilon}}_\beta$ is expressed as

$$\frac{\partial^2 \sigma(\omega)}{\partial \omega' \, \partial \Omega'} = \frac{\alpha^4 \omega}{\omega'} \sum_{\beta=1,2} \left(\sum_{i,f} D_{0if\beta} + \sum_{F} C_{0IF\beta} \right). \quad (1)$$

Each $D_{if\beta}$ term describes a single scattering path which goes from the initial (ground) state $|0\rangle$ to the final atomic state $|f\rangle$ via the intermediate atomic state $|i\rangle$:

$$|G_0 J_0\rangle + \gamma(\omega, \hat{\boldsymbol{\epsilon}}_0) \rightarrow |G_i J_i\rangle \rightarrow |G_f J_f\rangle + \gamma(\omega', \hat{\boldsymbol{\epsilon}}_\beta). \quad (2)$$

According to the Kramers-Heisenberg formula [30], the term is given by

$$D_{0if\beta} = \frac{1}{[J_0]} \sum_{M_f, M_0} \left\{ \frac{\delta(E_f + \omega' - E_0 - \omega)}{(E_i - E_0 - \omega)^2 + \Gamma_i^2/4} \left| \sum_{M_i} \left(\langle G_f J_f M_f | \sum_n \mathbf{p}_n \cdot \hat{\boldsymbol{\epsilon}}_\beta | G_i J_i M_i \rangle \langle G_i J_i M_i | \sum_n \mathbf{p}_n \cdot \hat{\boldsymbol{\epsilon}}_0 | G_0 J_0 M_0 \rangle \right) \right|^2 \right\}. \quad (3)$$

In Eq. (3), E is the energy of the state, J and M are the total angular momentum and its projection on the quantization axis, respectively, whereas G is used to denote the remaining quantum numbers. The sum runs over all single electron momenta $\mathbf{p}_n$ in the atom. The photoionization

$$|G_0 J_0\rangle + \gamma(\omega, \hat{\boldsymbol{\epsilon}}_0) \rightarrow |G_I J_I\rangle + e^-(\mathbf{k}) \rightarrow |G_F J_F\rangle + \gamma(\omega', \hat{\boldsymbol{\epsilon}}_\beta) + e^-(\mathbf{k}), \quad (4)$$

also leads to the emission of a photon. The continuum contribution to the cross section going through the intermediate ionic state $|I\rangle$ and ending in the final ionic state $|F\rangle$ is given by

$$C_{0IF\beta} = \frac{1}{[J_0]} \sum_{\substack{M_F, M_0 \\ m_s}} \int d^3 k \left\{ \frac{\delta(E_F + \epsilon + \omega' - E_0 - \omega)}{(E_I + \epsilon - E_0 - \omega)^2 + \Gamma_I^2/4} \left| \sum_{M_I} \left(\langle G_F J_F M_F | \sum_n \mathbf{p}_n \cdot \hat{\boldsymbol{\epsilon}}_\beta | G_I J_I M_I \rangle \langle G_I J_I M_I; \mathbf{k} m_s | \sum_n \mathbf{p}_n \cdot \hat{\boldsymbol{\epsilon}}_0 | G_0 J_0 M_0 \rangle \right) \right|^2 \right\}. \quad (5)$$

The propagation vector of the ejected electron is denoted by $\mathbf{k}$. The summation includes both spin projections. The form assumes that the continuum electron does not affect the photon emission from the intermediate ionic state.

Performing summation over the magnetic quantum numbers of the intermediate state, the resonant contribution appears as

$$D_{0if\beta} = \frac{9}{4[J_0]} B(J_0, J_i, J_f; \hat{\boldsymbol{\epsilon}}_0, \hat{\boldsymbol{\epsilon}}_\beta) \, \delta(E_f + \omega' - E_0 - \omega)$$

$$\times \frac{(E_i - E_f)(E_0 - E_i)(\mathrm{gf})_{if}(\mathrm{gf})_{0i}}{(E_i - E_0 - \omega)^2 + \Gamma_i^2/4}. \quad (6)$$

The angular factors

$$B = \frac{[J_f]}{[J_0]} \sum_{M_0, M_f} \left| \sum_{M_i} (-1)^{M_i} \times \sum_{q, q'} b_{q'} a_q \begin{pmatrix} J_i & 1 & J_f \\ M_i & q' & -M_f \end{pmatrix} \right.$$

$$\left. \times \begin{pmatrix} J_0 & 1 & J_i \\ M_0 & q & -M_i \end{pmatrix} \right|^2 \quad (7)$$

depend on the total angular momenta of the atomic states involved in the reaction path and on the polarization of the incoming and outgoing photons,

$$\hat{\boldsymbol{\epsilon}}_0 = \sum_{q=-1}^{1} a_q \hat{\boldsymbol{\epsilon}}^q, \quad \hat{\boldsymbol{\epsilon}}_\beta = \sum_{q'=-1}^{1} b_{q'} \hat{\boldsymbol{\epsilon}}^{q'}. \quad (8)$$

Weighted oscillator strengths are expressed by the corresponding reduced matrix elements of the dipolar transition operator $\mathbf{O}^1$ [31]:

$$(\mathrm{gf})_{uv} = \frac{2}{3} \frac{|\langle v \| \mathbf{O}^1 \| u \rangle|^2}{(E_u - E_v)}. \quad (9)$$

Similarly, it is not difficult to show that the continuum contribution can be written as

$$C_{0IF\beta} = \frac{9}{4[J_0]} \int_0^\infty d\epsilon \left\{ \delta(E_F + \epsilon + \omega' - E_0 \right.$$

$$- \omega) \frac{(E_I - E_F)(E_0 - E_I - \epsilon)(\mathrm{gf})_{IF}}{(E_I + \epsilon - E_0 - \omega)^2 + \Gamma_I^2/4}$$

$$\left. \times \sum_j A(J_0, J_I, J_F, j; \hat{\boldsymbol{\epsilon}}_0, \hat{\boldsymbol{\epsilon}}_\beta) \left(\frac{\partial f_j}{\partial \epsilon} \right)_{0,I\epsilon} \right\}. \quad (10)$$

The summation runs incoherently over the ejected electron angular momenta j, and the integration is over the ejected electron energy ϵ. Note that $C_{0IF\beta}$ is only different from zero when

4

$$\omega' < E_0 + \omega - E_F, \qquad (11)$$

producing a characteristic cutoff on the high energy side of the continuum emission line. The explicit form of angular factors A and oscillator strength densities $\partial f_j/\partial \epsilon$ in the last line of Eq. (10) depends on the description of the continuum state $|G_I J_I M_I; \mathbf{k}\rangle$. Inserting Eqs. (6) and (10) into Eq. (1) results in an expression that matches the cross section formula [21]. The effect of the finite final state lifetimes Γ_f and Γ_F is accounted for by replacing delta functions by the normalized Lorentzians [30]. Finally, the shape of the measured spectrum crucially depends on the spectral density $dP(\omega_0; \omega)/d\omega$ of the incoming photon beam with the nominal energy ω_0 and on $dS(\omega_1; \omega')/d\omega'$, the spectrometer transmission function at the nominal detection energy ω_1; the measured photon yield

$$I(\omega_0, \omega_1) = \sum_{i,f} I_{if}(\omega_0, \omega_1) + \sum_F I_{IF}(\omega_0, \omega_1) \qquad (12)$$

is in fact proportional to

$$\int d\omega \frac{dP(\omega_0; \omega)}{d\omega} \int d\omega' \frac{dS(\omega_1; \omega')}{d\omega'} \frac{\partial^2 \sigma(\omega)}{\partial \omega' \partial \Omega'}. \qquad (13)$$

We further rewrite Eqs. (6) and (10) in the form convenient to parameterize the measured photon yield. Each resonant path depends on five parameters: Energy differences $E_i - E_0$, $E_i - E_f$, lifetimes Γ_i and Γ_f of the corresponding intermediate and final atomic state, respectively, and on the resonance emission strength:

$$f_{0if} = \frac{9\alpha^4 \Gamma_f}{8\pi[J_0]} (gf)_{if} (gf)_{0i} (E_i - E_f)(E_0$$
$$- E_i) \sum_{\beta=1}^{2} B(J_0, J_i, J_f; \hat{\boldsymbol{\epsilon}}_0, \hat{\boldsymbol{\epsilon}}_\beta). \qquad (14)$$

Assuming a Gaussian shape of the transmission function, the following fitting form describes $I_{if}(\omega_0, \omega_1)$, the resonant contribution to the photon yield:

$$f_{0if} \int \int d\omega \, d\omega' \left[\frac{\omega}{\omega'} \exp\left(-\frac{(\omega - \omega_0)^2}{2\sigma_p^2} - \frac{(\omega' - \omega_1)^2}{2\sigma_s^2}\right) [(E_i$$
$$- E_0 - \omega)^2 + \Gamma_i^2/4]^{-1} [(E_f - E_0 - \omega + \omega')^2 + \Gamma_f^2/4]^{-1} \right]. \qquad (15)$$

The integration range of ω and ω' can be restricted to a narrow interval around ω_0 and ω_1 which depends on the instrumental broadening σ_p and σ_s, respectively. Similarly, at fixed solid angle, each continuum contribution can be parametrized by two energy differences $E_I - E_0$ and $E_I - E_f$, the lifetimes Γ_I and Γ_F of the intermediate and final core hole, respectively, and by $(\partial f/\partial \epsilon)_{0IF\epsilon}$, the continuum emission strength,

$$\left(\frac{\partial f}{\partial \epsilon}\right)_{0IF\epsilon} = \frac{9\alpha^4 \Gamma_F}{8\pi[J_0]} (gf)_{IF} (E_I - E_F)(E_I + \epsilon - E_0)$$
$$\times \sum_j \left(\frac{\partial f_j}{\partial \epsilon}\right)_{0,I\epsilon} \sum_{\beta=1}^{2} A(J_0, J_I, J_F, j; \hat{\boldsymbol{\epsilon}}_0, \hat{\boldsymbol{\epsilon}}_\beta). \qquad (16)$$

It turns out, as shown later, that this quantity is a smoothly decreasing function of ϵ. To properly describe fluorescence yield across the threshold, this energy dependence is taken into account by representing the continuum path strength by a simple rational function,

$$\left(\frac{\partial f}{\partial \epsilon}\right)_{0IF\epsilon} = \frac{1 + a\epsilon}{1 + b\epsilon} \left(\frac{\partial f}{\partial \epsilon}\right)_{0IF0}, \qquad (17)$$

where $(\partial f/\partial \epsilon)_{0IF0}$ is the continuum path strength at the threshold ($\epsilon = 0$), and a and b are two new target-dependent parameters. The expression for $I_{IF}(\omega_0, \omega_1)$, the photon yield emitted via the continuum path, is then

$$\left(\frac{\partial f}{\partial \epsilon}\right)_{0IF0} \int \int \frac{d\omega \, d\omega' \, \omega}{\omega'} \exp\left[-\frac{(\omega - \omega_0)^2}{2\sigma_p^2} \right.$$
$$\left. -\frac{(\omega' - \omega_1)^2}{2\sigma_s^2} \right] K(E_0, E_I, E_F, \omega, \omega'), \qquad (18)$$

where

$$K = \int_0^{\epsilon_\infty} d\epsilon \left(\frac{1 + a\epsilon}{1 + b\epsilon}\right) [(E_I + \epsilon - E_0 - \omega)^2 + \Gamma_I^2/4]^{-1} [(E_F - E_0$$
$$+ \epsilon + \omega' - \omega)^2 + \Gamma_F^2/4]^{-1} \qquad (19)$$

is an analytical function, and $\epsilon_\infty \gg \omega_0 - E_0 + E_I$. Except in the vicinity of the threshold jump, the continuum emission strength changes slowly with the energy of the ejected electron and can be taken as a constant in the narrow energy region centered at $\epsilon_c = \omega_0 - E_0 + E_I$, which gives the largest contribution to the integral over ϵ in Eq. (10).

Fitting formulas (15) and (18) cannot be reduced further in general since the integrals involved cannot be solved in the closed form. Nevertheless, the parametrization can be still applied to our problem if ω and ω' are discretized and the convolution integrals are replaced by appropriate summations.

IV. CALCULATIONS

A. Discrete states

We have calculated *ab initio* the majority of parameters to generate a set of x-ray Raman spectra across the L_3 threshold. The energies of intermediate states $[2p_{3/2}]5d-7d, 6s$ ($J = 1$) and of the corresponding spectator final states $[3d_{5/2,3/2}, 4d_{5/2,3/2}]5d-7d, 6s$ ($J = 1, 2$) with respect to the ground state were calculated by the Dirac-Fock model [31]. Using a single configuration approximation, the eigenenergies obtained by this relativistic code (Table I) are close to the values reported by more elaborate many-body relativistic calculations [32]. We have also calculated the weighted oscillator strengths for dipole transitions among pairs of dis-

5

crete states with radial orbitals of the intermediate state configuration. In Table I, the (gf) values are given in the Coulomb gauge (the length form) [33].

The z-axis was set along the polarization direction of the incoming photon beam, so that

$$\hat{\boldsymbol{\epsilon}}_0 = \hat{\boldsymbol{\epsilon}}^0, \quad \hat{\boldsymbol{\epsilon}}_{1,2} = \frac{1,i}{\sqrt{2}}(\hat{\boldsymbol{\epsilon}}^{-1} \mp \hat{\boldsymbol{\epsilon}}^1). \quad (20)$$

Summing up the angular factors (7) for both final polarizations as required by Eq. (14), one obtains

$$\sum_{\beta=1}^{2} B(0,1,1;\hat{\boldsymbol{\epsilon}}_0,\hat{\boldsymbol{\epsilon}}_\beta) = \sum_{\beta=1}^{2} B(0,1,2;\hat{\boldsymbol{\epsilon}}_0,\hat{\boldsymbol{\epsilon}}_\beta) = \frac{1}{3}, \quad (21)$$

while the emission exactly along the initial polarization is forbidden for $J_f=0$. The data input for the resonant part of Eq. (1) was completed by taking the recommended linewidths of intermediate and final states from the literature [20]: $\Gamma_{i,I}=2.82$ eV for $[2p_{3/2}]$ state and $\Gamma_{f,F}=0.6(0.08)$ eV and $0.59(0.1)$ eV for $[3d_{5/2}]([4d_{5/2}])$ and $[3d_{3/2}]([4d_{3/2}])$ final states, respectively. The linewidth of the inner-shell excited states was assumed independent of the type of the occupied upper orbital.

B. Continuum

It is more difficult to estimate the continuum part because in principle the photoelectron can be involved in the subsequent decay of the ion, taking away some part of the angular momentum. Below we follow the approach of Caldwell and Zare [34] and neglect completely the anisotropic interaction of the photoelectron with the ion. The intermediate state is approximated by

$$|G_I J_I M_I;\mathbf{k},m_s\rangle \approx \frac{1}{\sqrt{N!}}\sum_P (-1)^P P |G_I J_I M_I\rangle |\mathbf{k},m_s\rangle, \quad (22)$$

where the photoelectron wave function $|\mathbf{k},m_s\rangle$ is expressed with spherical waves,

$$(2\pi)^{-3/2}\left[4\pi\sum_{lm} i^l e^{-i\delta_l} T_l(\epsilon,r) Y_{lm}^*(\hat{\mathbf{k}}) Y_{lm}(\hat{\mathbf{r}})\right]|sm_s\rangle, \quad (23)$$

with limited number of nonzero terms due to angular momentum conservation and parity change in the photoabsorption,

$$\mathbf{J}_0 + \mathbf{j}_0 = \mathbf{J}_I + \mathbf{l} + \mathbf{s}, \quad (-1)^{l+1} = \Pi_0 \Pi_I. \quad (24)$$

In Eq. (24), $\mathbf{j}_0$ is the angular momentum of the incident photon and $\mathbf{s}$ is the electron spin. The initial (ground) state is expressed as an antisymmetrized product of an electron orbital, from which an electron is ejected, and the rest of the atom

$$|G_0 00\rangle \approx \frac{1}{\sqrt{N!}}\sum_P (-1)^P P |L_I s J_I - M_I\rangle |L_I s J_I M_I\rangle. \quad (25)$$

The simplest approximation is obtained if the ejected electron does not disturb the rest of the atom in the course of photoemission, so that the ionic part remains

$$|G_I J_I M_I\rangle = |L_I s J_I M_I\rangle. \quad (26)$$

The atomic matrix element [the last factor of Eq. (5)] then reduces to the sum of one-electron matrix elements

$$\sum_{lm} \sqrt{\frac{2}{\pi}} i^l e^{-i\delta_l} Y_{lm}^*(\hat{\mathbf{k}}) \langle Y_{lm}(\hat{\mathbf{r}}) T_l(\epsilon,r), sm_s|z|L_I s J_I - M_I\rangle. \quad (27)$$

We proceed by decomposing the initial electron orbital into the sum of spin-orbit products and combine this with the expression for the matrix element between the ionic bound states. Upon integration over the solid angle of the ejected electron, Eq. (5) becomes

$$C_{0IF\beta} = \frac{\omega^2 |\langle F\|\mathbf{O}^1\|I\rangle|^2}{[J_0]} \int_0^\infty \frac{d\epsilon}{(E_I + \epsilon - E_0 - \omega)^2 + \Gamma_I^2/4} \sum_l [l]$$
$$\times \begin{pmatrix} l & 1 & L_I \\ 0 & 0 & 0 \end{pmatrix}^2 f_l(L_I,J_I,J_F;\hat{\boldsymbol{\epsilon}}_0,\hat{\boldsymbol{\epsilon}}_\beta) \langle T_l(\epsilon)|r|P_{nL_I}\rangle^2. \quad (28)$$

The radial orbital from which the electron was ejected is denoted by P_{nL_I}. The geometrical factors f_l are given by

$$\frac{[L_I,J_F]}{2} \sum_{m,m_s} \left\{ \begin{pmatrix} L_I & 1/2 & J_I \\ -m & -m_s & m+m_s \end{pmatrix} \begin{pmatrix} l & 1 & L_I \\ -m & 0 & m \end{pmatrix} \right.$$
$$\left. \times \left[\begin{pmatrix} J_I & 1 & J_F \\ m+m_s & -1 & -M_F \end{pmatrix} \mp \begin{pmatrix} J_I & 1 & J_F \\ m+m_s & 1 & -M_F \end{pmatrix} \right] \right\}^2, \quad (29)$$

where the upper and lower sign apply when $\beta=1$ and $\beta=2$, respectively. We therefore establish the following connection of the model with parametrization (16):

$$\left(\frac{\partial f}{\partial \epsilon}\right)_{0IF\epsilon} = \frac{9\alpha^4 \Gamma_F}{8\pi[J_0]}(\text{gf})_{IF}(E_F - E_I)(E_I + \epsilon - E_1)\frac{2}{3}\omega_0 \sum_l \left\{ [l] \right.$$
$$\left. \times \begin{pmatrix} l & 1 & L_I \\ 0 & 0 & 0 \end{pmatrix}^2 \langle T_l(\epsilon)|r|P_{nL_I}\rangle^2 \sum_{\beta=1}^{2} f_l(L_I,J_I,J_F;\hat{\boldsymbol{\epsilon}}_0,\hat{\boldsymbol{\epsilon}}_\beta) \right\}. \quad (30)$$

The radial matrix elements were calculated for different ϵ above the threshold employing radial waves $T_l(\epsilon)$ which were calculated in the presence of $[2p_{3/2}]$ potential [35]. In our case, $J_0=0$, $n=2$, $L_I=1$, and $J_I=3/2$, so that only s and d waves describe the ejected electron. The latter contribution is the dominant one:

$$|\langle T_l(0)|r|P_{2p}\rangle|^2 = \begin{cases} 8.5 \times 10^{-6}, & l=0, \\ 1.27 \times 10^{-4}, & l=2. \end{cases} \quad (31)$$

The strength of the continuum emission (16) depends most strongly on the energy of the ejected electron through the oscillator strength density, which in turn depends on the magnitude of the radial matrix elements. As shown by the calculation, the square of the matrix element smoothly decreases for about 15% when ϵ changes from 0 to 8 eV. The rational function (17) with $a=0.155$ and $b=0.229$ takes this energy dependence into account and reproduces the calcu-
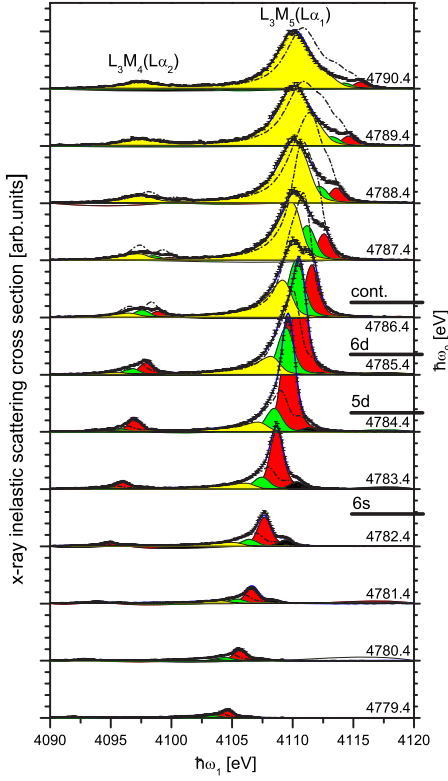
FIG. 2. (Color online) Comparison of the measured, the fitted (black line, blue - color online) and the calculated (dot-dashed line) x-ray inelastic scattering cross sections as a function of emitted energy ω_1 for 12 different incoming photon energies ω_0 in the $L_3M_{5,4}$ energy region. The spectra are decomposed into four different intermediate state components, as given by the fit: $[2p_{3/2}]6s$ state: black fill color; $[2p_{3/2}]5d$: dark gray fill (red - color online); $[2p_{3/2}](n \geq 6d)$: medium gray fill (green - color online) and $[2p_{3/2}]$: light gray fill (yellow - color online). Horizontal lines denote energy positions of the resonances and of the threshold.

lated trend up to 20 eV above the Xe L_3 threshold. It also reproduces well the slope of the measured absorption coefficient above the threshold, where the contribution of the resonant single excitations is negligible (Fig. 4).

V. RESULTS

A. $L_3M_{5,4}$ energy region

Since both polarization components generate the same spectral shape in our experimental geometry, the relative intensities of recorded emission lines are not modified even if the crystal (detector) response depends on the polarization of the scattered (detected) photon. A series of twelve spectra generated by the calculated parameters (Table I) are normalized to experimental data by a single scaling factor to match the measured intensity of L_3M_5 line about 5 eV above the L_3 threshold. Large discrepancies with the measured data may be seen in Fig. 2, although the model parameters values—such as energy differences and path strengths—are approximately correct. This shows the potential of the x-ray Raman data set to test the theoretical predictions in detail.

We have also fitted the model parameters to reach a minimum χ^2 for the full series of measured spectra. In $L_3M_{5,4}$ energy region the model accounts for six resonant (via $[2p]_{3/2}6s$, $[2p]_{3/2}5d$, and $[2p]_{3/2}nd$, $6 \leq n \leq n_0$) and two continuum paths which end with the $3d_{5/2}$ or $3d_{3/2}$ hole. The contribution of the ns Rydberg series was neglected. Also the electric quadrupole excitations were neglected as suggested by relatively small value of the calculated weighted oscillator strength for the ground state to $[2p_{3/2}]4f_{5/2,7/2}$ transition: 3.9×10^{-10}. Assuming that the quantum defect approximation [36] is valid for $n \geq 6$, the contribution of the nd Rydberg progression was parametrized by the threshold energy E_I, and by the energy $E_i(6)$ and resonant path strength $f_{0if}(6)$ of the intermediate $[2p]_{3/2}6d$ state: Taking that the fluorescence decay branching ratio does not depend on n, we set

$$E_i(n) = E_I - \left(\frac{6-\sigma}{n-\sigma}\right)^2 [E_I - E_i(6)],$$

$$f_{0if}(n) = \left(\frac{6-\sigma}{n-\sigma}\right)^3 f_{0if}(6), \qquad (32)$$

and sum up the terms (15) up to $n_0 = 50$. The energy difference of each Rydberg intermediate and Rydberg final state was fixed to the corresponding $L_3M_{5,4}$ emission line energy. A quantum defect $\sigma = 2.4$ was inserted above because this value is consistent with the calculated ratio $f_{0if}(6)/f_{0if}(7)$, and with the calculated energies $E_i(6)$, $E_i(7)$, and E_I. Although the final $[2p]_{3/2}6d$ parameter values depend slightly on the particular choice of σ, the fitting results for the lower lying states are stable in this respect. The continuum path strength was accounted for by treating $(\partial f/\partial \epsilon)_{0IF0}$ as a free parameter, while a and b parameters in Eq. (17) were kept fixed at the calculated values.

The final fit is presented in Fig. 2 and agrees very well with the measured data (reduced $\chi^2 = 2.13$). There is one overall scaling parameter for the whole series of spectra (exactly the same scaling factor is used for the calculated spectra). The fit also gave the best values for Γ_I, σ_p and σ_s (Sec. II). When comparing the converged parameter values to the previously published level energies (Table I), the threshold energy position is found at about 0.4 eV higher value than reported by [24] and insignificantly below the value reported by Ohno and LaVilla [29] (−0.1 eV). The discrete state energies are shifted likewise, they are about 0.4 eV higher with respect to [24], which indicates a difference in the energy calibration of the incoming light. There is still a good optical match with the $Z+1$ atom Rydberg progression of Cs $5p^6(^1S)nl$, which justifies the use of the quantum defect approximation (32). The $[3d_{5/2,3/2}]6s, 5d$ final state energies were found not to differ significantly from the corresponding intermediate state energy lowered by the $L_3M_{5,4}$ continuum line energy, respectively.

If the obtained relative energy positions essentially confirm the results of the fitting procedure performed by Breinig et al. [29], also regarding the $[2p_{3/2}]6s$ state which was not clearly detected in the past, the important result of this work is the determination of the relative intensities of various Raman path strengths. It turns out that the $5d$ mediated path is

more probable with respect to ($\geq 6d$) and $6s$ paths (1:0.25:0.06) than expected from the calculated ratio (1:0.48:0.12). It seems that the $[2p_{3/2}]5d$ contribution to the x-ray inelastic scattering is stronger than predicted by a simple single configuration model. Also, the intensity of the continuum path ending in $[3d_{3/2}]$ state versus $[3d_{5/2}]$ state was found slightly larger (0.09) than predicted by the calculations (0.07).

With the converged parameter values, one is also able to reproduce well the measured absorption profile, from which the (Victoreen) pre-edge contribution was subtracted [Fig. 4(b)]. Since here the oscillator strengths of ground state excitations are substituted by the corresponding emission strengths, it seems that the fluorescence decay branching ratio for various excited states is essentially not changed when moving across the threshold. The sole presence of an inner hole dictates the branching ratio value. An advantage of the x-ray Raman spectroscopy in terms of the spectral resolution is evident by comparing Figs. 2 and 4(b): The unresolved absorption signal becomes partially resolved in x-ray inelastic scattering spectra, allowing more precise spectroscopic work.

B. $L_3N_{5,4}$ energy region

We have also recorded the $L_3N_{5,4}$ x-ray Raman spectra at ten different incoming photon energies around the L_3 edge (Fig. 3). The intermediate states involved are the same as in the case of $L_3M_{5,4}$ lines, so we kept their energy positions as well as the energy profile of the incoming photon beam fixed and varied only the path strengths and the final state energies. According to the theory the flux of the scattered light in the continuum line is now 8.4 times lower, but the Raman spectra are slightly better resolved, mainly on account of the increased lifetime of the final states with the $4d$ hole ($\Gamma_f \approx 0.1$ eV). The best fit was achieved (reduced $\chi^2 = 1.79$) by using a slightly narrower Gaussian representation of the spectrometer transmission function than in the case of $L_3M_{5,4}$ lines. This seems contrary to expectations since $L_3N_{5,4}$ lines correspond to smaller Bragg angle. Accidentally, the Bragg angle for $L_3M_{5,4}$ measurements on quartz ($10\bar{1}0$) is very close to 45°, where the complete extinction of one polarization component occurs after the reflection on the crystal, so that the spectrometer transmission function could have been additionally broadened due to this reason. Also, the shape of the spectrometer function has probably changed; it seems sharper in the $L_3N_{5,4}$ energy region, as hinted by Fig.3.

The fit placed the final state energy of $[4d]_{5/2}5d$ exactly onto 65.54 eV, the value reported long ago by the high resolution electron energy loss spectroscopy [37]. Upon subtraction of the $L_3N_{5,4}$ emission energies [29] from previously determined $[2p]_{3/2}$ threshold energy, the final state energies match very well the published values of $[4d]_{5/2,3/2}$ threshold energies [37]. Also in the case of $L_3N_{5,4}$ transitions, the intensity of the $5d$ spectator line relative to the continuum is again underestimated by about 20% by the theory, while the $6d$ line is overestimated by approximately the same factor. The relative ratio of the continuum $(L_3N_4)/(L_3N_5)$ lines as given by the fit is higher than the calculated value, although
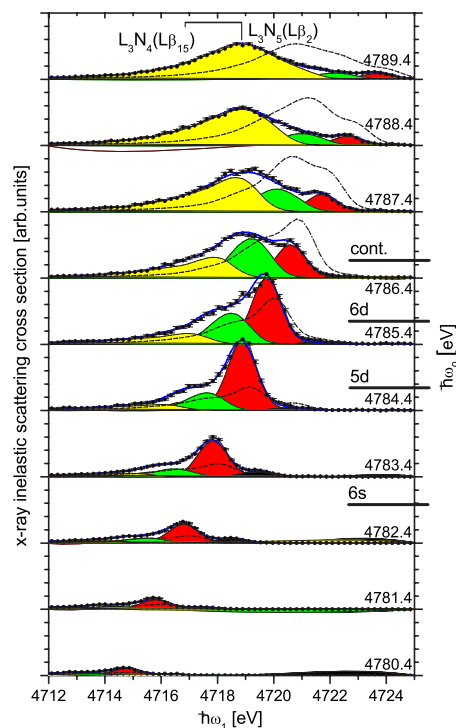

FIG. 3. (Color online) Comparison of the measured, the fitted (black line, blue - color online), and the calculated (dotted line) x-ray inelastic scattering cross sections as a function of emitted energy ω_1 for 10 different incoming photon energies ω_0 in the $LN_{5,4}$ energy region. The spectra are decomposed into four different intermediate state components as given by the fit, keeping the intermediate state energy positions (and notation) the same as in Fig. 2.

the result is now less reliable due to the smaller energy separation of the doublet.

C. $L_3O_{2,3}$ excitations

The first structure in the absorption spectrum above the L_3 threshold [Fig. 4(b)] shows up as a broad peak centered at 4798 eV and reaches about 3% of the intensity of the threshold jump [6]. It is attributed to a group of $[2p_{3/2}5p]nln'l'$ states. To investigate for the presence of x-ray Raman fluorescence yield mediated by these doubly excited states, additional fourteen spectra were recorded to cover the incoming photon energy range 4791.4–4804.4 eV in 1 eV steps. After the normalization and self-absorption correction, the dominant $[3d_{5/2}]$ continuum path contribution was subtracted from each measured spectrum [Fig. 4(a)]. To lower the statistical uncertainty, each spectral residue was shifted to align in energy the signals originating from the same resonance below the threshold. This negative energy shift just compensates the increase of the incoming photon energy so that the resonant Raman signal of a given intermediate state appears always at the same energy position. The shifted spectral residua were summed up to generate a constant atomic state spectrum (CAS) in analogy to the constant ionic state spectrum (CIS), commonly used in the resonant Auger spectroscopy. The strongest group of lines in CAS [Fig. 4(c)] originates from the singly excited intermediate states $[2p_{3/2}]nd$,
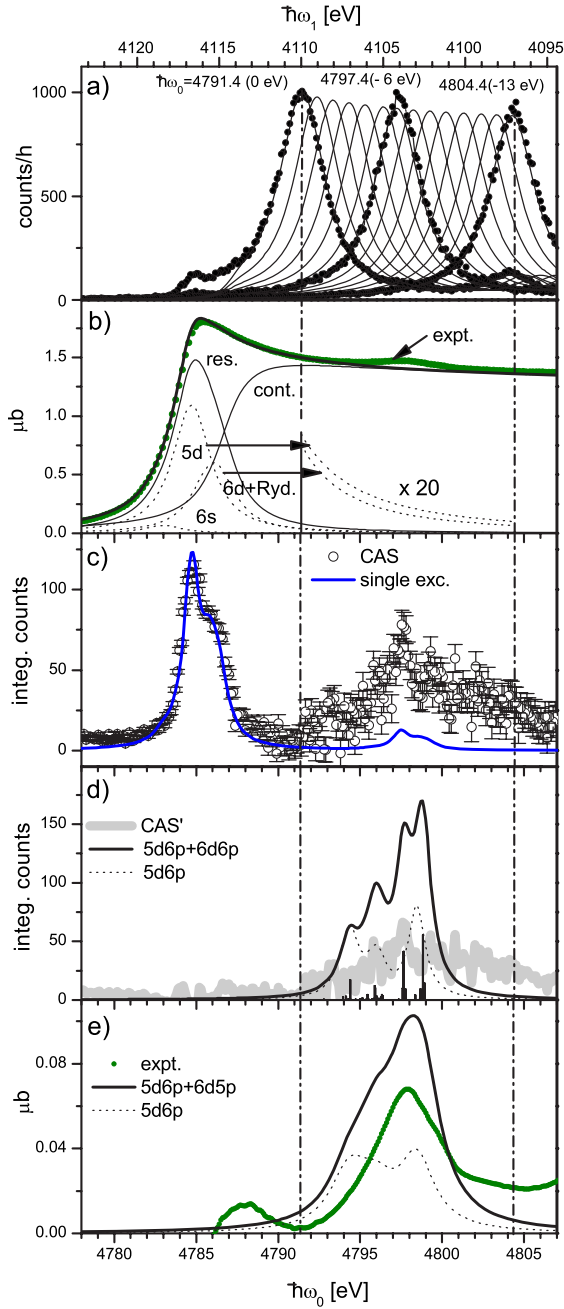
FIG. 4. (Color online) (a) L_α spectra backshifted in energy and the corresponding continuum contribution propagated according to Eq. (17). For clarity only 3 of 14 measured spectra are shown. (b) Measured absorption spectrum (circles, green - color online) reconstructed from the converged energies and relative emission strengths of singly excited states (res) and continuum (cont). A blowup of the tail is shown in the region of doubly excited states. (c) CAS spectrum with overlapping contributions of singly and doubly excited states. The former is modeled by the line (black, blue - color online). (d) CAS spectrum of doubly excited states only compared to single configuration (dotted line) and double configuration (full line) calculation convoluted with the experimental +final state broadening. (e) Absorption structure which belongs to doubly excited states is extracted from the measurement and compared to the two calculations convoluted with natural linewidth of the $2p_{3/2}$ hole.

for which the signal is strongly diminished due to the off-resonance sampling; the intensity is expected to be just a few percent of the full resonance emission strength (3.1%, 4.3%, and 5.6% for $[2p]_{3/2}6s$, $[2p]_{3/2}5d$, and $[2p]_{3/2}(\geq 6d)$ states, respectively). The ratios areestimated by the lineshape integral over the selected energy range [shown in Fig. 4(b)] divided by the lineshape integral over all the energies. On the other hand, we expect that doubly excited states are represented in CAS by a major part of their full emission strengths because the lowest (highest) incoming photon energy in the set is well below (above) the energies where most of their signal appears in the absorption.

The below-threshold contribution is convoluted by the previously determined Voigt profile to account for the experimental and final state broadening and nicely reproduces lower energy part of the CAS spectrum (Fig. 4(c)). Accidentally, the L_3M_4 part of the singly excited states overlaps in CAS with the signal of doubly excited states: Since energies of the latter with respect to the threshold approximately coincide with the $L_3M_5 - L_3M_4$ energy difference, the resonant part of L_3M_4 due to the singly excited states moves over the L_3M_5 continuum line together with the L_3M_5 resonant part of doubly excited states when the incoming photon energy is changed. Figure 4(d) represents CAS with the signal of singly excited states subtracted. This is finally compared to the calculated spectrum which was generated from the oscillator strength distribution of $[2p_{3/2}5p](5d6p + 6d6p)$ states. In short, the oscillator strengths were obtained from the dipole matrix elements between the states for which the radial orbitals were separately optimized for the initial ground state and for the final singly or doubly excited states with the $2p_{3/2}$ hole. The overlap of the nonorthogonal orbitals appearing in the calculation accounts for the monopole excitation of the outer electron which accompanies the main dipole transition [38]. The calculated multiplet structure was convoluted with the Voigt profile and shifted in energy to match the slope of the CAS in Fig. 4(d). The assumption about the relative oscillator strengths reliably representing relative emission strengths of singly and doubly excited states [vice-versa to assumption underlying Fig. 4(b)] fixes the scaling between the two and leads to the conclusion that the calculated CAS overestimates the experimental signal. Also, a plot of the calculated oscillator strengths of doubly excited states, broadened by the $2p$ hole linewidth reproduces the position of the measured maximum in the absorption, but predicts too high intensity. The calculated shape of the absorption peak is approximately right, and was improved when two configurations were included into the calculation. This seems to converge to the four-peak multiplet structure of $[2p5p]nln'l'$ states, which is just hinted in the measured CAS spectrum.

VI. CONCLUSIONS

We have measured a series of high resolution x-ray spectra in the energy region of Xe $L_3M_{5,4}$ and $L_3N_{5,4}$ lines. The target was excited by photons, and experimental broadening was kept below 40% of the natural linewidth of the intermediate $[2p_{3/2}]$ state. Using a suitable parametrization, we were able to directly access energies and emission strengths of the

lowest resonances below the L_3 threshold, in particular $[2p]_{3/2}6s$ state was clearly resolved for the first time. The converged parameter values are consistent with the $L_3M_{5,4}$ and $L_3N_{5,4}$ series of spectra, and indicate stronger excitation of $[2p]_{3/2}5d$ state than expected from the calculation. The shape of the absorption spectra across the threshold is well reproduced by inserting the path strengths instead of the corresponding oscillator strengths, which shows that the fluorescence decay branching ratio in the threshold energy region has a fairly constant value. Upon subtraction of the dominant continuum component, the L_3M_5 signal from doubly excited $L_3O_{2,3}$ states was also detected. Using the x-ray resonant Raman scattering in this case may finally lead to better resolved spectra of inner-hole doubly excited states, but for definite conclusions, experimental data with better statistics is required.

[1] J. M. Esteva *et al.*, J. Phys. B **16**, L263 (1983).

[2] R. D. Deslattes, R. E. LaVilla, P. L. Cowan, and A. Henins, Phys. Rev. A **27**, 923 (1983).

[3] S. J. Schaphorst A. F. Kodre, J. Ruscheinski, B. Crasemann, B. T. Aberg, J. Tulkki, M. H. Chen, Y. Azuma, and G. S. Brown, Phys. Rev. A **47**, 1953 (1993).

[4] M. Deutsch and P. Kizler, Phys. Rev. A **45**, 2112 (1992).

[5] K. Zhang, E. A. Stern, J. J. Rehr, and F. Ellis, Phys. Rev. B **44**, 2030 (1991).

[6] I. Arčon, A. Kodre, M. Štuhec, D. Glavič-Cindro, and W. Drube, Phys. Rev. A **51**, 147 (1995).

[7] Y. Ito, A. M. Vlaicu, T. Tochio, T. Mukoyama, M. Takahashi, S. Emura, and Y. Azuma, Phys. Rev. A **57**, 873 (1998).

[8] S. Svensson *et al.*, Phys. Scr. **14**, 141 (1976).

[9] K. Hämäläinen, D. P. Siddons, J. B. Hastings, and L. E. Berman, Phys. Rev. Lett. **67**, 2850 (1991).

[10] G. S. Brown, M. H. Chen, B. Crasemann, and G. E. Ice, Phys. Rev. Lett. **45**, 1937 (1980).

[11] A. Kivimäki, A. NavesdeBrito, S. Aksela, H. Aksela, O. P. Sairanen, A. Ausmees, S. J. Osborne, L. B. Dantas, and S. Svensson, Phys. Rev. Lett. **71**, 4307 (1993).

[12] R. Camilloni, M. Zitnik, C. Comicioli, K. C. Prince, M. Zacchigna, C. Crotti, C. Ottaviani, C. Quaresima, P. Perfetti, and G. Stefani, Phys. Rev. Lett. **77**, 2646 (1996).

[13] P. Lablanquie F. Penent, R. I. Hall, H. Kjeldsen, J. H. D. Eland, A. Muehleisen, P. Pelicon, Z. Smit, M. Zitnik, and F. Koike, Phys. Rev. Lett. **84**, 47 (2000).

[14] P. Eisenberger *et al.*, Phys. Rev. Lett. **36**, 623 (1976).

[15] C. F. Hague, M. Tronc, Y. Yanagida, A. Kotani, J. H. Guo, C. Sathe, Phys. Rev. A **63**, 012511 (2000).

[16] J. H. Guo, Y. Luo, A. Augustsson, J. E. Rubensson, C. Sathe, H. Agren, H. Siegbahn, and J. Nordgren, Phys. Rev. Lett. **89**, 137402 (2002).

[17] H. Hayashi, Y. Udagawa, W. A. Caliebe, and C. C. Kao, Phys. Rev. B **66**, 033105 (2002).

[18] J. P. Rueff, L. Journel, P. E. Petit, and F. Farges, Phys. Rev. B **69**, 235107 (2004).

[19] M. A. MacDonald, S. H. Southworth, J. C. Levin, A. Henins, R. D. Deslattes, T. LeBrun, Y. Azuma, P. L. Cowan, and B. A. Karlin, Phys. Rev. A **51**, 3598 (1995).

[20] J. L. Cambell and T. Papp, At. Data Nucl. Data Tables **77**, 1 (2001).

[21] T. Åberg and J. Tulkki, in *Atomic Inner-Shell Physics*, edited by Bernd Crasemann, (Plenum Press, New York, 1985, Chap. 10), pp. 419–463.

[22] G. B. Armen, S. H. Southworth, J. C. Levin, U. Arp, T. LeBrun, and M. A. MacDonald, Phys. Rev. A **56**, R1079 (1997).

[23] M. Alagia *et al.*, Phys. Rev. A **71**, 012506 (2005).

[24] M. Breinig, M. H. Chen, G. E. Ice, F. Parente, B. Crasemann, and G. S. Brown, Phys. Rev. A **22**, 520 (1980).

[25] M. Kavčič *et al.*, Nucl. Instrum. Methods Phys. Res. B **222**, 601 (2004).

[26] O. Mauron, J. C. Dousse, S. Baechler, M. Berset, Y. P. Maillard, P. A. Raboud, and J. Hoszowska, Phys. Rev. A **67**, 032506 (2003).

[27] F. Gel'mukhanov and H. Ågren, Phys. Rep. **312** (1999).

[28] R. D. Deslattes *et al.*, Rev. Mod. Phys. **75**, 35 (2003).

[29] M. Ohno and R. E. LaVilla, Phys. Rev. A **45**, 4713 (1992).

[30] J. J. Sakurai, *Advanced Quantum Mechanics* (Addison-Wesley, Reading, MA, 1967).

[31] K. G. Dyall *et al.*, Comput. Phys. Commun. **55**, 425 (1989).

[32] T. Mooney, E. Lindroth, P. Indelicato, E. G. Kessler, Jr., and R. D. Deslattes, Phys. Rev. A **45**, 1531 (1992).

[33] I. P. Grant, J. Phys. B **7**, 1458 (1974).

[34] C. D. Caldwell and R. N. Zare, Phys. Rev. A **16**, 255 (1977).

[35] W. F. Perger, Z. Halabuka, and D. Trautmann, Comput. Phys. Commun. **76**, 250 (1993).

[36] C. M. Theodorescu *et al.*, J. Phys. B **26**, 4019 (1993).

[37] G. C. King *et al.*, J. Phys. B **10**, 2479 (1977).

[38] O. Zatsarinny, Comput. Phys. Commun. **98**, 235 (1996).